Journal of Alloys and Compounds, *187* (1992) 317–330
JALCOM 320

The formation of a barrier oxide layer on a Zr–2.5wt.%Nb alloy during corrosion in high temperature pressurized water

Yuquan Ding and Derek O. Northwood
Engineering Materials Group, Mechanical Engineering Department, University of Windsor, Windsor, Ont. N9B 3P4 (Canada)

(Received March 20, 1992)

Abstract

Zr–2.5wt.%Nb alloy specimens, and for comparative purposes pure zirconium, were exposed to a pressurized lithiated water environment containing 4.8 g of LiOH per litre of H_2O at 300 °C, and the oxides at the oxide–metal interface were characterized by transmission electron microscopy (TEM) and scanning electron microscopy (SEM). TEM and SEM studies show that the barrier oxide layer formed on a Zr–2.5wt.%Nb alloy in the aqueous environment has a complex structure. The structure of the barrier oxide layer on Zr–2.5wt.%Nb consists of two parts, namely one resulting from corrosion of grain boundary phases and the other resulting from corrosion of the bulk α-Zr grains. The former consists mainly of tetragonal ZrO_2 crystallites. The latter consists of amorphous or mosaic layers and transformed tetragonal ZrO_2. In contrast, the oxide at or near the oxide–metal interface on pure zirconium specimens exposed to the same environment consists only of amorphous and mosaic structures which are relatively continuous.

1. Introduction

A Zr–2.5Nb alloy where the composition is given in weight per cent and other zirconium alloys such as the Zircaloys are used for the manufacture of nuclear reactor core components such as fuel cladding and pressure tubing because of their low neutron absorption cross-section, high strength and high corrosion resistance under reactor operating conditions [1]. The corrosion and associated hydrogen ingress behaviour of zirconium alloys are often considered in terms of the effects of a "barrier layer" at the oxide–metal interface which can significantly reduce hydrogen ingress and oxidation rates with time, as long as the barrier layer remains intact and protective. The questions that needed to be answered with respect to this barrier layer were as follows: (i) what is it and (ii) is there really such a layer? There are relatively few reports of studies on the oxide close to the oxide–metal interface in zirconium and its alloys, especially Zr–2.5Nb, as seen using scanning electron microscopy (SEM) and transmission electron microscopy (TEM) analysis techniques [2–10].

Garzarolli *et al.* [8] have described the microstructure of the oxide–metal interface for the three different types of oxide structure, namely (i) uniform

0925-8388/92/$5.00

oxides formed in water, (ii) uniform oxides formed in oxygen and (iii) a nodular oxide formed in steam on Zircaloy specimens. The main structure at the interface for the uniform oxide formed in water and for the nodular oxide formed in steam is a columnar structure of monoclinic ZrO_2. This monoclinic columnar structure is considered to be formed because, as noted by Murase and Kato [11], moisture markedly accelerates crystallite growth for both monoclinic and tetragonal ZrO_2 and facilitates the tetragonal-to-monoclinic phase transformation. The normal structure formed by oxidation in oxygen primarily consists of monoclinic ZrO_2 as well as some tetragonal ZrO_2 and an amorphous structure. In an investigation of Zr–2.5Nb, Warr *et al.* [6] also observed that amorphous regions were formed not only at the oxide–metal interface but also fairly generally at oxide grain boundaries. Recently, Wadman and Andren [9] used atom probe analysis and TEM to study thin oxide layers grown in air and boiling water on Zircaloy-4 specimens and found that the oxide layers 10 nm thick were partially amorphous and contained small oxide crystallites. The oxygen content of the amorphous layers was low, less than 50 at.%.

In order to determine whether a barrier oxide layer exists on Zr–2.5Nb, which would be responsible for preventing, or at least reducing, hydrogen ingress, it is important to obtain information on the nature of the oxide film, particularly that which is closest to the oxide–metal interface. In the present work, we have exposed Zr–2.5Nb pressure tube specimens, and for comparative purposes pure zirconium, to a pressurized lithiated water environment at 300 °C for short (pre-transition) and long (post-transition) times and have studied the formation of a barrier oxide layer using TEM and SEM techniques.

2. Experimental details

2.1. Details of corrosion tests and specimens

The starting material was commercial grade Zr–2.5Nb pressure tubing supplied by Ontario Hydro in the cold-worked-and-stress-relieved condition. Specimens were sections cut directly from pressure tubing with dimensions of approximately 20 mm × 15 mm × about 4 mm (thickness) of pressure tubing. The corrosion–hydriding tests were carried out in high pressure (8.65 MPa), high temperature (300 °C) static autoclaves of 50 cm^3 capacity. A LiOH concentration of 4.8 g of LiOH per litre deionized water (H_2O) was used in order to accelerate the corrosion reaction. The chemical analysis of the tubing and full details of corrosion tests can be found in ref. 10. The pure zirconium specimens were arc-melted crystal-bar zirconium and were used as a baseline material for comparative purposes.

2.2. Preparation of specimens for transmission electron microscopy and scanning electron microscopy examination

Specimens were first cut from the corroded Zr–2.5Nb pressure tubing using a low speed diamond saw as shown in ref. 10. In order to determine

the nature of any changes in the barrier oxide layer with exposure time, two groups of specimens were chosen, namely those exposed for 40 h (pre-transition) and those exposed for 480 h (post-transition). Typical weight gain (oxidation) *vs.* exposure time results for this batch of Zr–2.5Nb specimens under these environmental conditions can be found in ref. 10.

The specimens for TEM and SEM examination included all three sections of pressure tubing, namely the axial–radial, radial–tangential and axial–tangential surfaces. Thin foil TEM specimens containing the oxide–metal interface were then prepared using an ion-milling technique that was modified from one originally developed by Moseley and Hudson [12]. The ion beam thinning was initially conducted from the metal side until the foil specimen was perforated at the edge [7]. The thin foil specimens were examined at 100 kV in a JEM-100CX microscope with a scanning attachment.

Full details of the SEM preparation techniques can be found in ref. 10. The SEM tapered cross-section technique is particularly designed to observe the oxide–metal interface structure. The SEM examination was performed on a Nanolab 7 scanning electron microscope.

3. Results

3.1. Scanning electron microscopy examination of the oxide close to the oxide–metal interface

Figures 1(a) and 1(b) are the SEM micrographs of tapered sections of pre- and post-transition specimens of Zr–2.5Nb with the oxide layers on the axial–radial surface. Figures 2(a) and 2(b) are SEM micrographs for the same specimens but with the oxide layers on the radial–tangential surface. Figures 3(a) and 3(b) are SEM micrographs for the same specimens but with the oxide layers on the axial–tangential surface. From Figs. 1–3, it can

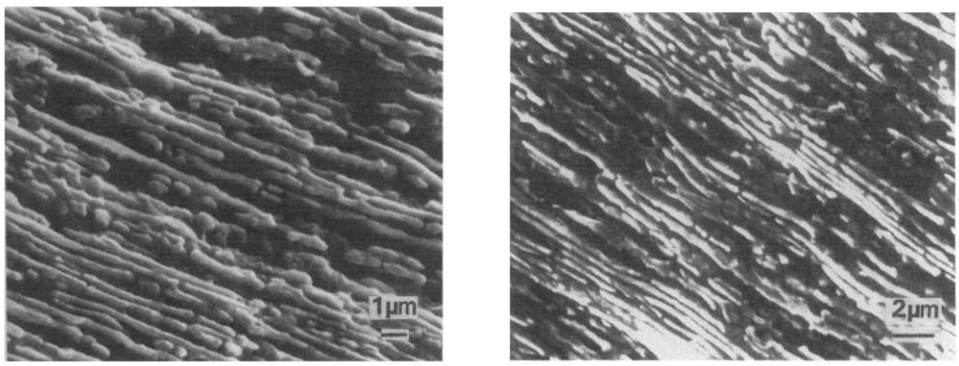

(a) (b)

Fig. 1. Topography of oxides formed at the oxide–metal interface for (a) pre-transition (40 h) and (b) post-transition (480 h) Zr–2.5Nb specimens exposed to pressurized lithiated water containing 4.8 g of LiOH per litre of H_2O at 300 °C (the oxide layer is on the axial–radial surface).

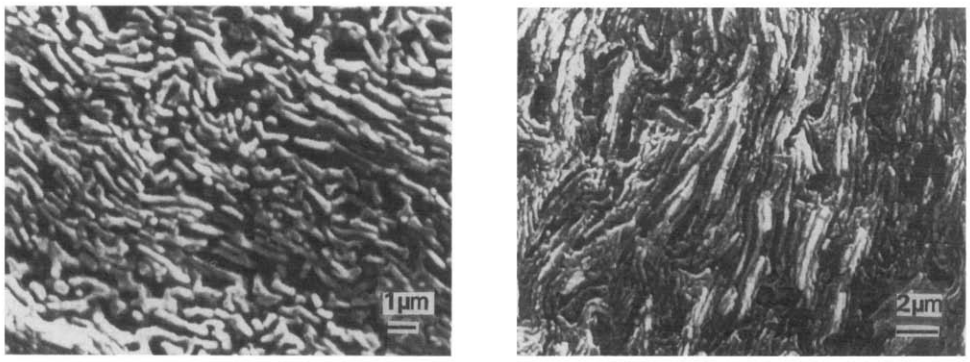

(a) (b)

Fig. 2. Topography of oxides formed at the oxide–metal interface for (a) pre-transition (40 h) and (b) post-transition (480 h) Zr–2.5Nb specimens exposed to pressurized lithiated water containing 4.8 g of LiOH per litre of H_2O at 300 °C (the oxide layer is on the radial–tangential surface).

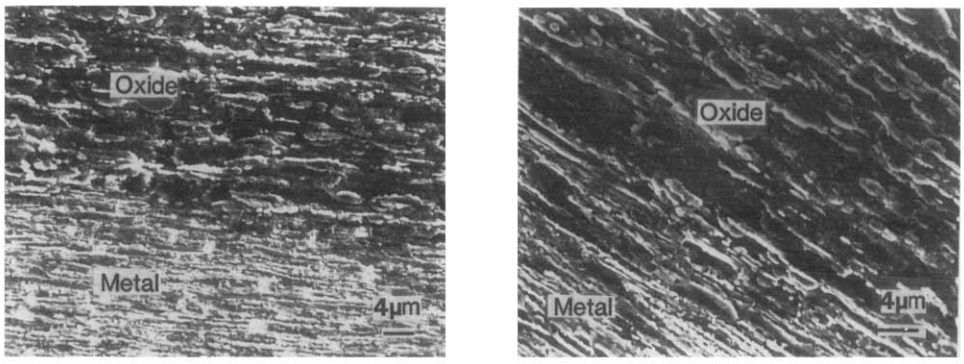

(a) (b)

Fig. 3. Topography of oxides formed at the oxide–metal interface for (a) pre-transition (40 h) and (b) post-transition (480 h) Zr–2.5Nb specimens exposed to pressurized lithiated water containing 4.8 g of LiOH per litre of H_2O at 300 °C (the oxide layer is on the axial–tangential surface).

be seen that the oxides formed in cold-worked Zr–2.5Nb pressure tubing in pressurized lithiated water at 300 °C are mainly extended along grain boundaries and are composed of many fine ZrO_2 grains. Oxidation in the specimens with different sections proceeds along grain boundaries in the same manner. Because of the different α-Zr grain sizes, shapes and orientations in the different sections, there are different grain boundary distributions on the different section faces, and corrosion can proceed at different rates. The underlying relationship between the structure of the metal and the oxidation pattern remains.

The preferred orientation of α-Zr grains in the arc-melted crystal-bar specimens is not pronounced as in Zr–2.5Nb pressure tubing specimens.

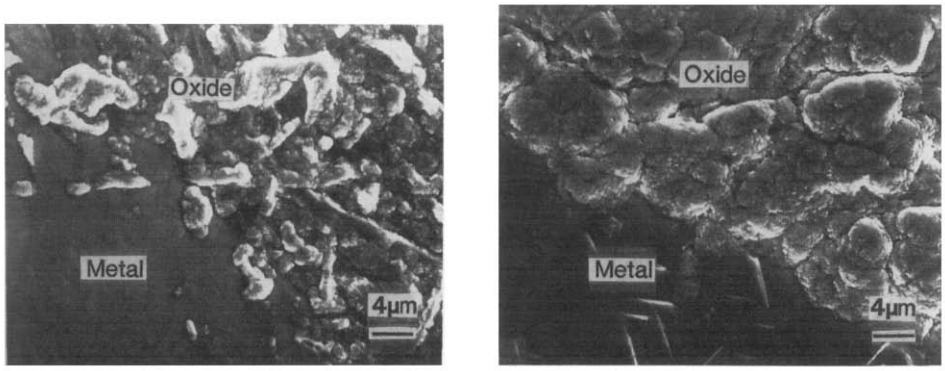

(a) (b)

Fig. 4. Topography of oxides formed at the oxide–metal interface for pure zirconium specimens exposed to pressurized lithiated water containing 4.8 g of LiOH per litre of H_2O at 300 °C for (a) a short corrosion time (40 h) and (b) a long corrosion time (480 h).

Figures 4(a) and (b) are typical SEM micrographs of oxides formed on a pure zirconium specimen after exposure for 40 h and 480 h respectively. The mismatch between the oxide lattice and the pure zirconium gives rise to stresses which may be relieved by the generation of the spherical clusters of "cauliflower-like" granules. As shown in Fig. 4(a), the oxide formed after a short corrosion time (40 h) has a "streaky" appearance and appears to be different from that formed after a long corrosion time (480 h). The structure of the oxide with the "streaky" appearance formed after a short corrosion time (40 h) can be seen better in a higher magnification micrograph (Fig. 5). The oxide close to the oxide–metal interface also has a "cauliflower-like" structure.

However, even for high magnification SEM, it was difficult to resolve the structure fully very close to the oxide–metal interface. This was accomplished using TEM techniques.

3.2. Transmission electron microscopy examination of the oxide close to the oxide–metal interface

3.2.1. Localized amorphous regions and mosaic structure

Figure 6 shows a localized amorphous region with fine equiaxed tetragonal crystallites (most are less than 10 nm in size) at the oxide–metal interface in a pre-transition Zr–2.5Nb specimen exposed for 40 h; the oxide layer is perpendicular to the axial direction of pressure tubing, *i.e.* it lies on the radial–tangential surface. The diffraction pattern (inset in Fig. 6) shows that the oxide structure at the oxide–metal interface is amorphous. Figure 7(a) is a micrograph of the oxide formed at the oxide–metal interface in a post-transition Zr–2.5Nb specimen exposed for 480 h; the oxide layer lies on the radial–tangential surface. Because of preferential ion beam thinning, there was no, or very little, oxide present in some areas of the specimen. On comparison of Figs. 2 and 7, it can be seen that morphology of the oxide

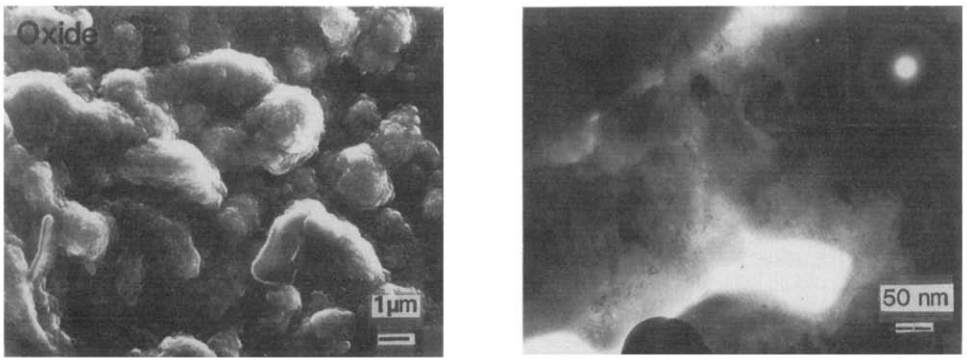

Fig. 5. Topography of oxides formed at the oxide–metal interface of a pure zirconium specimen exposed to pressurized lithiated water containing 4.8 g of LiOH per litre of H_2O at 300 °C for a short corrosion time (40 h).

Fig. 6. Amorphous region with small tetragonal ZrO_2 crystallites at the oxide–metal interface for a pre-transition Zr–2.5Nb specimen exposed to pressurized lithiated water containing 4.8 g of LiOH per litre of H_2O at 300 °C for 40 h.

front as observed using SEM is consistent with that of the oxide front observed using SEM. Note that the oxide front shown in Fig. 2 is formed along grain boundaries. The thinner oxide shown in Fig. 7 is also formed along grain boundaries. The detail of oxide structure can be better seen at higher magnification micrographs (Figs. 7(b) and 7(c)). The oxide close to the oxide–metal interface has a mosaic structure consisting of very small crystallites (5–30 nm). Mismatch between the oxide lattice and the metal gives rise to stresses which may be relieved by the generation of mosaic structures whose lattices are slightly twisted or tilted with respect to one another.

Figures 8(a) and 8(b) are typical TEM micrographs of a pure zirconium specimen exposed for a long corrosion time (480 h). Selected-area diffraction (SAD) patterns, *e.g.* the inset in Fig. 8(a), show that the oxide shown in Fig. 8(a) has an amorphous structure. Figure 8(b) shows that the oxide close to the oxide–metal interface consists of smaller spherical clusters of "cauliflower-like" granules than those observed using SEM; compare with Fig. 4(b). Each of the smallest clusters has a mosaic structure whose lattice are slightly twisted or tilted with respect to one another (Fig. 8(b)). Pure zirconium specimens exposed to a 300 °C pressurized lithiated water environment show a different behaviour from that of the Zr–2.5Nb specimens. Since the pure zirconium specimens do not have the complex grain boundary structures as in the Zr–2.5Nb alloys, preferential oxidation at the grain boundaries is not observed.

3.2.2. Crystalline oxide formed near the oxide–metal interface

Figures 9(a) and 9(b) are the typical micrographs of pre- and post-transition Zr–2.5Nb specimens respectively with oxide layers parallel to the axial direction of pressure tubing, *i.e.* the oxide is in the axial–radial surface.

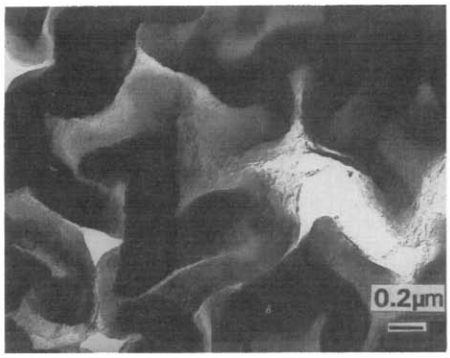

(a)

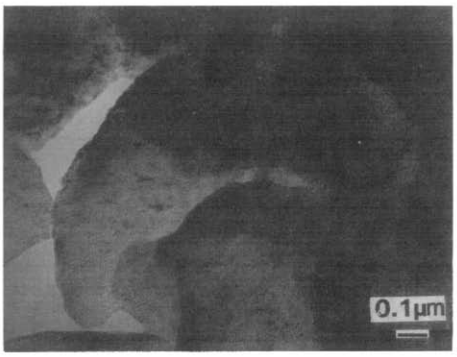

(b)

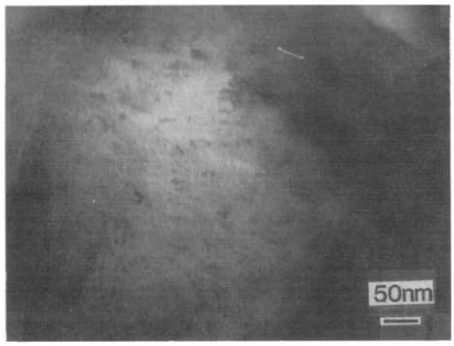

(c)

Fig. 7. TEM micrographs of the oxide formed at the oxide–metal interface in a post-transition Zr–2.5Nb specimen exposed to pressurized lithiated water containing 4.8 g of LiOH per litre of H_2O at 300 °C for 480 h.

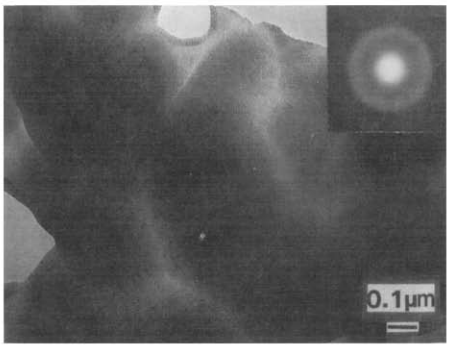

(a)

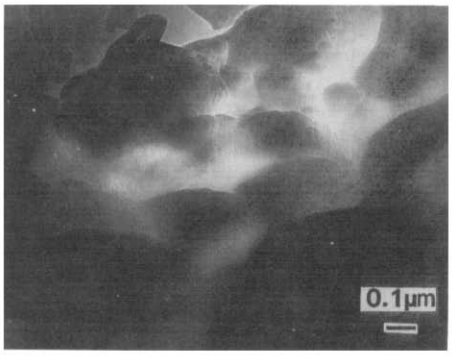

(b)

Fig. 8. Typical (a) amorphous and (b) mosaic structures at the oxide–metal interface for a pure zirconium specimen exposed to pressurized lithiated water containing 4.8 g of LiOH per litre of H_2O at 300 °C for 480 h.

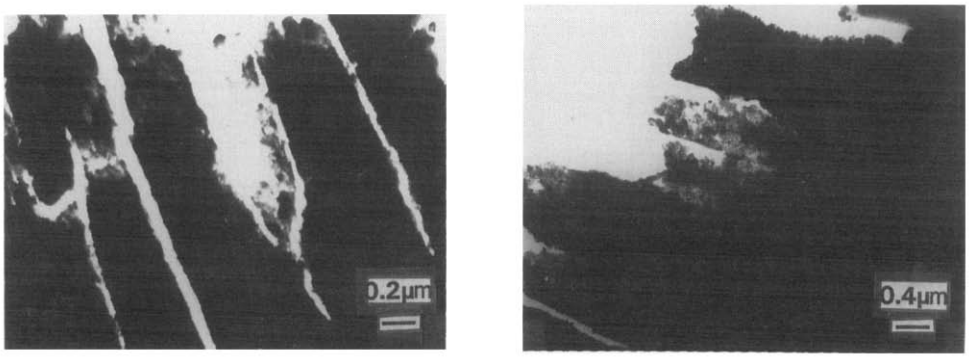

(a) (b)

Fig. 9. TEM micrograph of the oxide–metal interface on (a) pre-transition and (b) post-transition Zr–2.5Nb specimens exposed to pressurized lithiated water containing 4.8 g of LiOH per litre of H_2O at 300 °C (the oxide layer is on the axial–radial surface).

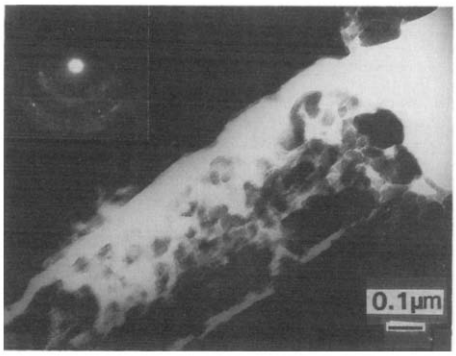

Fig. 10. TEM micrograph of oxide formed at the oxide–α-Zr interface on a pre-transition Zr–2.5Nb specimen exposed to pressurized lithiated water containing 4.8 g of LiOH per litre of H_2O at 300 °C (the oxide layer is on the axial–radial surface).

The underlying metal structure of cold-worked Zr–2.5Nb alloy consists of long elongated grains of α-Zr with filaments of β-Zr at the grain boundaries [13]. Fine, relatively equiaxed grains of ZrO_2 are formed "on" the α-Zr grains. The ZrO_2 grains are of relatively uniform size ranging from about 30 to 50 nm in size (Fig. 10). There was no ZrO_2 present at the regions between the α-Zr grains but this is probably a result of preferential ion beam thinning at these locations. The SAD pattern (inset in Fig. 10), showed that the oxide at the oxide–α-Zr interface was tetragonal ZrO_2. The microstructure of the oxide–metal interface where the oxide layer is perpendicular to the axial direction of pressure tubing, *i.e.* the oxide is on the radial–tangential surface, is shown in Figs. 11(a) and 11(b). The oxide formed at the α-Zr grain boundaries has a variable grain size with grains as small as 10 nm (Fig. 11(a)). Some areas of the oxide formed at the grain boundaries, usually far from the oxide–metal interface, contained cracks and pores (Figs. 11(a)

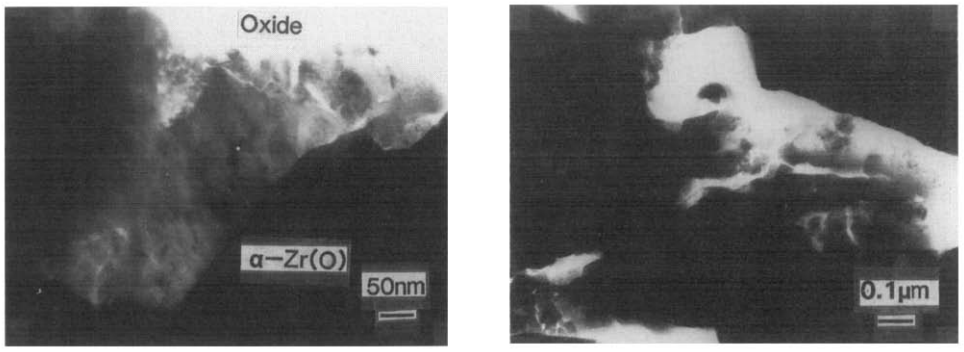

(a) (b)

Fig. 11. TEM micrographs showing that the oxide formed at the oxide–metal interface on a Zr–2.5Nb specimen exposed to pressurized lithiated water containing 4.8 g of LiOH per litre of H_2O at 300 °C for 40 h has a variable grain size with some areas with grains as small as 20 nm (the oxide layer is on the radial–tangential surface).

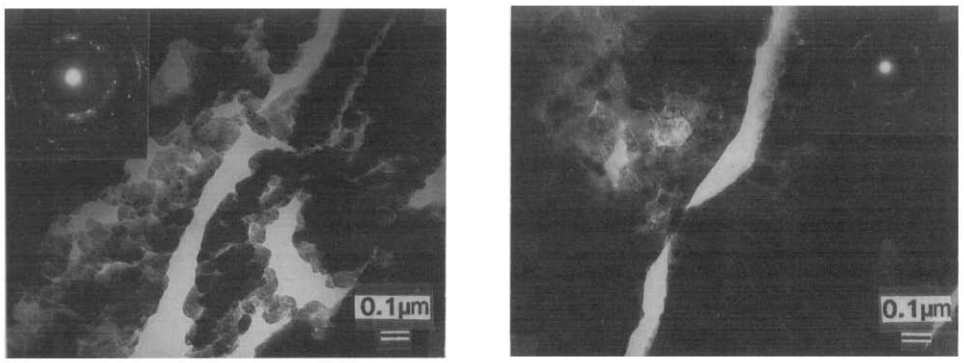

Fig. 12. TEM micrograph of oxide (tetragonal and monoclinic ZrO_2) formed at the α-Zr grain boundaries on a post-transition specimen (the oxide layer is on the radial–axial surface).

Fig. 13. TEM micrograph of oxide (tetragonal ZrO_2) formed at the oxide–α-Zr interface on a post-transition specimen (the oxide layer is on the radial–axial surface).

and 11(b)). For the post-transition specimens, although the bulk of the ZrO_2 grains near the α-Zr grain boundaries are fine (30–50 nm), some of the grains are much larger than 50 nm (Fig. 12). The SAD pattern of the oxide area shown in Fig. 12 indicates that the oxide is a mixture of tetragonal and monoclinic ZrO_2. Figure 13 is another typical TEM micrograph of the oxide at the oxide–metal interface for a post-transition specimen. The SAD pattern (inset in Fig. 13) shows that the oxide is tetragonal ZrO_2. As shown in Figs. 12 and 13, there are two typical structures for the oxide close to the interface in post-transition specimens.

4. Discussion

4.1. Formation of barrier oxide layer on Zr–2.5Nb alloy

Several theories [14, 15] have been proposed to describe the kinetics and mechanisms of the corrosion behaviour in zirconium and its alloys. Some of the viewpoints are contradictory, often because of poor understanding of the microstructure of the barrier oxide layer at the oxide–metal interface.

As shown in Fig. 6 for a pre-transition specimen, we observed amorphous regions at the oxide–metal interface where very fine (smaller than 10 nm) tetragonal ZrO_2 crystallites formed. An SEM examination of a post-transition specimen showed that the microstructure of metal close to the oxide–metal interface was different from that far away from the interface; the α-Zr grains close to the interface appeared "larger" than the α-Zr grains far from the interface [16]. The solubility limit of oxygen in α-Zr, which is much larger than that of oxygen in β-Zr, is 29 at.%. During oxidation, oxygen dissolution takes place simultaneously with the growth of oxide, so that a metal zone rich in oxygen forms beneath the oxide layer. Therefore there is an intermediate oxygen-rich layer in the metal (α-Zr) close to the oxide–metal interface. The formation of amorphous regions may be related to kinetics of this intermediate layer formation.

It has been known for some time that the initial film which forms on tantalum, and on other metals such as aluminium, is amorphous rather than crystalline at low temperatures and/or low current densities [17–20]. There are at least two processes by which an amorphous anodic tantalum oxide film may be crystallized: (i) by heating at 800 °C; (ii) by holding at temperatures from 0 to 100 °C in the presence of a strong electric field. The crystallization of amorphous anodic Ta_2O_5 films has been found to be influenced by the temperature, the applied voltage, the condition of the metal surface and the impurity content of the metal. The oxidation of cold-worked Zr–2.5Nb pressure tubing in pressurized lithiated water at 300 °C proceeds first along grain boundaries at which there are β-Zr and its decomposition products and then continues on α-Zr grains [10]. Most of impurities in cold-worked Zr–2.5Nb, such as iron, magnesium, aluminium, chromium, hafnium and titanium, are concentrated at the grain boundaries. These impurities can act as nucleation sites. Because the oxide formed during the aqueous corrosion of Zr–2.5Nb for long times is white and porous, lithiated water is probably able to penetrate much closer to the oxide–metal interface [21, 22]. The crystallization process is significantly facilitated by aqueous solution at grain boundaries. Therefore the oxide formed at the grain boundaries in cold-worked Zr–2.5Nb, which contains β-Zr and its decomposition products together with impurities, consists mainly of crystallites rather than the amorphous phase.

As the oxidation of cold-worked Zr–2.5Nb pressure tubing in pressurized lithiated water then proceeds on α-Zr grains, a different corrosion mechanism is operative. The amorphous regions that we see in Fig. 6 are most probably a result of corrosion of α-Zr grains. This amorphous layer most probably has a structure with oxygen anion vacancies [9]. Since fresh oxide is formed

at the oxide–metal interface by the inward migration of oxygen anions for zirconium and its alloys, the outer layers of the oxide are those first formed. As the oxidation process proceeds, oxide at the oxide–metal interface is continuously replaced by fresh oxide. As well as oxidation, several other kinetic processes are occurring, in particular phase transformations in ZrO_2 which affect the structure of the barrier oxide layer formed at the oxide–metal interface. The nucleation of ZrO_2 crystallites within the amorphous phase, which is assisted by impurities in the metal, the particular condition of the metal surface and compressive stresses in the oxide, and the subsequent growth of these crystallites result in the formation of a mosaic structure. The mosaic structure consists of tetragonal ZrO_2 crystallites. The tetragonal, rather than the monoclinic, structure is attributed to the fine grain size of the ZrO_2 and the compressive stresses developed at the oxide–metal interface. Low valence niobium oxide and oxygen vacancies can also stabilize tetragonal ZrO_2 at the oxide–metal interface down to temperatures as low as room temperature. After further oxidation of the metal, the fine ZrO_2 crystallites in the mosaic structure gradually increase in size and become equiaxed tetragonal ZrO_2 grains. As long as the grain size of ZrO_2 remains smaller than some critical size, and/or the compressive stresses are larger than some critical pressure value, ZrO_2 continues to have the tetragonal structure. As any individual ZrO_2 layer moves away from the interface, the compressive stresses decrease rapidly. As the compressive stresses decrease and the grain size increases through the thickness of the oxide as one moves away from the oxide–metal interface, the tetragonal ZrO_2 is transformed to monoclinic ZrO_2. Because the surface energy of monoclinic ZrO_2 is larger than that of tetragonal ZrO_2, monoclinic ZrO_2 grains grow easily in one direction, *e.g.* along the C axis direction of tetragonal ZrO_2 with the largest plane interval (*i.e.* with large surface energy), and develop a columnar structure. Ganzarolli *et al.* [8] and other early work [23–25] has provided evidence for the columnar crystallite morphology in oxides formed on zirconium and its alloys. Therefore the sequence of structural changes undergone by the oxide is first from an amorphous phase to a mosaic structure, then to equiaxed tetragonal ZrO_2 and finally to monoclinic ZrO_2. The amorphous and mosaic structures formed during the corrosion of α-Zr grains in Zr–2.5Nb are similar to those formed during the corrosion of pure zirconium.

4.2. Structure of the barrier oxide layer formed at the oxide–metal interface

It has been known for many years that the oxide films on zirconium and its alloys during thermal oxidation were largely crystalline and were mainly monoclinic ZrO_2. Although it is generally agreed that the barrier oxide acts as a protective layer, the structure of the barrier oxide layer formed very close to the oxide–metal interface has not been understood very well.

In the commercial Zr–2.5Nb pressure tubing, a satisfactory corrosion resistance is obtained in tubing which is made by extrusion at 850 °C (in the α-Zr + β-Zr region), cold working and stress relieving (autoclaving). The

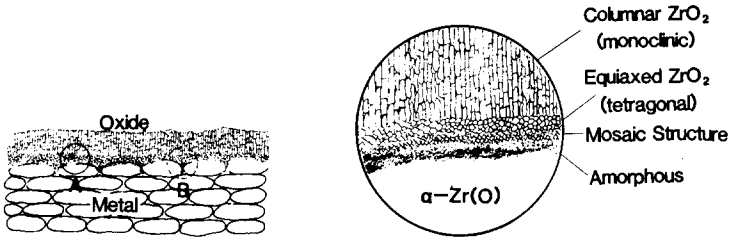

(a) (b)

Fig. 14. (a) Schematic illustration of the structure of the barrier oxide layer formed during the aqueous corrosion of Zr–2.5Nb showing that it consists of two parts: (i) one from corrosion of grain boundary phases (region B) and (ii) the other from corrosion of α-Zr grains (region A). (b) Magnified view of region A.

structure of such pressure tubing consists of elongated α-Zr grains and a grain boundary network of metastable β-Zr that contains 20 wt.% Nb [26]. During corrosion of cold-worked Zr–2.5Nb pressure tubing, there are two possible mechanisms: (i) grain boundary phase corrosion and (ii) bulk α-Zr grain corrosion; see schematic illustration in Fig. 14. In regions such as B in Fig. 14(a), the oxide formed from the oxidation of impurities or grain boundary phases, *e.g.* mixed oxides such as $6ZrO_2 \cdot Nb_2O_5$, have a variable grain size with some grains as small as 10 nm and others larger than 50 nm (Figs. 11 and 12). Some areas of the oxide formed from grain boundary phases, usually far from the oxide–metal interface, contained cracks and pores. These areas can become short-circuit paths for the diffusion of oxygen anions to the oxide-metal interface. At high LiOH concentrations, for example in a solution of 4.8 g of LiOH per litre of H_2O solution such as in these studies, short-circuit diffusion at grain boundaries produces a significant increase in corrosion rates. The oxide, which is very close to the oxide–metal interface and is formed from α-Zr grains, has an amorphous or mosaic structure, as shown in Figs. 6 and 7. The amorphous layer is at the oxide–metal (α-Zr) interface, immediately adjacent to which is α-Zr(O) (α-Zr(O) indicates α-Zr with a high interstitial oxygen content) below (Fig. 14(b)). Because in pure zirconium, h.c.p. α-Zr is stable at temperatures up to 862 °C and there are no complex grain boundary structures as in the Zr–2.5Nb, there is no preferential oxidation at the grain boundaries but rather the amorphous and mosaic structures form as a relatively continuous film. The localized amorphous and mosaic structures formed from α-Zr grains in Zr–2.5Nb (*e.g.* in regions such as A in Fig. 14) are similar to those formed on pure zirconium, but they are not continuous because of the different oxide formed at the grain boundaries which contain the β phase and impurities.

5. Conclusions

TEM and SEM studies show the structure of a barrier oxide layer at the oxide–metal interface in the Zr–2.5Nb specimens exposed to a pressurized

lithiated water environment containing 4.8 g of LiOH per litre of H_2O consists of amorphous, mosaic and tetragonal ZrO_2 layers. Amorphous and mosaic structures, which are similar to those formed in pure zirconium specimens, arise mainly from the corrosion of bulk α-Zr grains in Zr–2.5Nb specimens. Tetragonal ZrO_2 arises from the corrosion of grain boundary phases and transformation of amorphous and mosaic structures formed from the corrosion of bulk α-Zr grains.

Acknowledgments

This work was supported by the Natural Science and Engineering Research Council of Canada (Operating Grant A4391), the Canadian Deuterium Uranium Owner's Group through Working Party 35, and the University Research Incentive Fund, Province of Ontario, Canada. Mr. John W. Robinson assisted with the corrosion tests and with the electron microscopy examinations.

References

1 C. E. Ells and W. Evans, *Can. Min. Metal. Bull.*, *74* (1981) 105.
2 J. E. Bailey, *J. Nucl. Mater.*, *8* (1963) 259.
3 R. A. Ploc, *J. Nucl. Mater.*, *28* (1968) 48.
4 B. Cox, *J. Aust. Inst. Met.*, *14* (1969) 123.
5 H. Stehle, F. Garzarolli, A. M. Garde and P. G. Smerd, in D. G. Franklin and R. B. Adamson (eds.), *Zirconium in the Nuclear Industry, Proc. 6th Int. Symp.* in *ASTM Spec. Tech. Publ. 824*, 1984, p. 483 (American Society for Testing and Materials, Philadelphia, PA).
6 B. D. Warr, A. M. Brennenstuhl, M. B. Elmoselhi, E. M. Rasle, N. S. McIntyre, S. B. Newcomb and W. M. Stobbs, *Conf. on Microscopy of Oxidation, Cambridge, UK, March 1990.*
7 Y. Ding and D. O. Northwood, *Proc. 23rd Annu. Meet. of the International Metallographic Society, Cincinnati, OH, July 1990, Microstruct. Sci., 19* (1991) in the press.
8 F. Garzarolli, H. Seidel, R. Tricot and J. P. Gros, in C. M. Eucken and A. M. Garde (eds.), *Zirconium in the Nuclear Industry, Proc. 9th Int. Symp.* in *ASTM Spec. Tech. Publ. 1132*, 1991, p. 395 (American Society for Testing and Materials, Philadelphia, PA).
9 B. Wadman and H.-O. Andren, in C. M. Eucken and A. M. Garde (eds.), *Zirconium in the Nuclear Industry, Proc. 9th Int. Symp. in ASTM Spec. Tech. Publ. 1132*, 1991, p. 461 (American Society for Testing and Materials, Philadelphia, PA).
10 Y. Ding and D. O. Northwood, *J. Mater. Sci.*, *27* (1992) 1045.
11 Y. Murase and E. Kato, *J. Am. Ceram. Soc.*, *66* (1983) 196.
12 P. T. Moseley and B. Hudson, *J. Mater. Sci.*, *99* (1981) 340.
13 R. G. Fleck, E. G. Price and B. A. Cheadle, in D. G. Franklin and R. B. Adamson (eds.), *Zirconium in the Nuclear Industry, Proc. 6th Int. Symp. in ASTM Spec. Tech. Publ. 824*, 1984, p. 88 (American Society for Testing and Materials, Philadelphia, PA).
14 B. Cox, *J. Nucl. Mater.*, *29* (1969) 50.
15 D. H. Bradhurst and P. M. Heuer, *J. Nucl. Mater.*, *37* (1970) 35.
16 Y. Ding and D. O. Northwood, Methods for preparation of cross-sectional SEM specimens and their application to corroded specimens of a zirconium alloy and TiN coated stainless steel, *Mater. Characterization*, (1992) in the press.
17 D. A. Vermilyea, *J. Electrochem. Soc.*, *1102* (1955) 207.
18 D. A. Vermilyea, *J. Electrochem. Soc.*, *104* (1957) 542.

19 D. J. Stirland and R. W. Bickness, *J. Electrochem. Soc.*, *106* (1959) 481.
20 M. J. Dignam, *J. Electrochem. Soc.*, *109* (1962) 184.
21 A. V. Manolescu, P. Mayer and C. J. Simpson, *Corrosion*, *38* (1982) 31.
22 Y. Ding and D. O. Northwood, Characterization of the oxides formed on Zr–2.5wt.%Nb during high temperature corrosion, *J. Alloys Comp.*, *179* (1992) 207.
23 B. Cox and A. Donner, *J. Nucl. Mater.*, *47* (1973) 72.
24 J. P. Pemsler, *J. Electrochem. Soc.*, *112* (1965) 447.
25 G. P. Airey and G. P. Sabol, *J. Nucl. Mater.*, *45* (1972/73) 60.
26 V. F. Urbanic and R. W. Gilbert, *IAEA Technical Committee Meet. on Fundamental Aspects of Corrosion of Zirconium-Base Alloys for Water Reactor Environments, Portland, OR, September 1989.*